Development of Linear-Element Boundary Element Method for Inverse Solution from Induced Far-Field Displacements to Reservoir Loading Source

Yu Zhao[1], Hong Li[1,2]*, Zhengzhao Liang[1], Hui Zhou[2], Bin Gong[3]

[1] *State Key Laboratory of Coastal and Offshore Engineering, Dalian University of Technology, Dalian, China*

[2] *State Key Laboratory of Geomechanics and Geotechnical Engineering, Institute of Rock and Soil Mechanics, Chinese Academy of Sciences, Wuhan, China*

[3] *Department of Civil and Environmental Engineering, Brunel University London, London UB8 3PH, UK*

* *Corresponding author, Email:* hong.li@dlut.edu.cn

Abstract: An inverse solution strategy using linear element of Boundary Element Method (BEM) was developed, which will become a novel application base to potentially reflect the equivalent mechanical effect around reservoir corresponding to CO_2 spreading during its injection process. Firstly, a linear-element BEM code was studied to improve the accuracy in analyzing the connection between induced ground minute deformations and underground inner loading. Secondly, the space regularization was adopted to deal with the ill-posed problem during the optimization to inverse problem solution. The boundary conditions of a near-field structure as active source were reversely figured out in an efficient numerical way based on its passive deformation that was sampled at a few specific positions at far field. Meanwhile, the effectiveness of linear-element BEM in solving inverse problems was demonstrated. Finally, based on the implementation of hydraulic fracturing in a coal seam in Alberta, Canada, the monitored data of its induced surface displacements was input to invert the equivalent internal pressure onto a re-opened fracture within

reservoir. The results show that the proposed inverse solution workflow and programmed algorithm are applicable to effectively guiding hydraulic fracturing interpretation so as to further facilitating coalbed methane recovery.

Key words: Solution to inverse problems; Linear element of Boundary Element Method; Space regularization; Ground surface displacement monitoring; Crack re-opening during fracturing

1. Introduction

It has become a major strategic goal for the world to achieve 'carbon peak' and 'carbon neutral' [1]. It is beneficial to economy and environment to strengthen clean Coalbed Methane development by tight reservoir fracturing stimulation, which shoulders the important mission of transition from coal to green resources in energy consumption structure [2]. CO_2 enhanced coalbed methane (CO_2-ECBM) is a technology to drive and displace CH_4 by taking advantage of the fact that CO_2 adsorption performs better than CH_4 [3] when CO_2 is injected into coal seams and adsorbed onto the micropore walls within coal matrix. The process of CO_2-ECBM can not only realize carbon sequestration, but also improve the gas production rate from low permeability reservoirs [4]. Engineering practice shows that ground surface minute tilting displacements and undulation caused by hydraulic fracturing can effectively reflect the underground crack opening and closure extent, injected fluid pressure and other mechanical aspects of migration [5]. The optimized inversion technique, which uses micro-tilt monitoring over the surface or along the far field bore-hole inner walls to interpret the mechanical effect of hydraulic fracturing, has been widely applied in the fields. However, the underground rock strata is assumed as homogeneous and isotropic as a whole and, therefore the optimized inverse solution based on fundamental analytic solutions is relatively

idealized. The method in this paper, however, based on infinite elastic solution, makes full use of the induced far-field deformation monitoring data, especially the formations can be numerically modeled in a more realistic way where the different properties of sedimentary geology is possible to be well represented, and high precision and fast calculation algorithms are programmed to realize numerical solution to inverse problems. The developed workflow is potential to inversely estimate the internal pressure within the facture communicative with bottom-hole perforations or spreading of pressure fluctuation inside reservoir by fluid injection. The technique is exploratory and there has been few precedents studying high-efficiency numerical solution to inverse problems for field application.

The BEM had evolved from boundary integral method. With the development of computer technology and the reference of finite element method, BEM has been gradually flourishing divided into direct and indirect methods. In 1967, Rizzo used the direct BEM and applied its two-dimensional analysis to engineering problems [6]. In 1976, Lachat and Waston [7] proposed the BEM effective for three-dimensional elastic analysis. In 1976, Crouch and Starfield [8] proposed the displacement discontinuity method, one of the indirect BEMs, which had been widely applicable in rock mass engineering since 1983 [9]. In 1978, Chinese scholars Du Qinghua and Yao Zhenhan from Tsinghua University initiated the research of BEM in engineering [10]. Feng Kang, Hu Haichang, He Guanggan and other researchers joined the researches of BEM. A great progress has been made in BEM application to hydraulic engineering geomechanics as well as other fields. Constant element [11], linear element [12,13], second-order element [14] and higher-order element [15] can be chosen and developed with regard to BEM programs. Due to the lack of a mature technology in rigorous error control, the orders of unit might form an impact on calculation

64 accuracy and efficiency [16,17]. Crouch published open-source programs constant element
65 Displacement Discontinuity Method (DDM) and Fictitious Stress Method (FSM) of indirect BEM
66 for analyzing elastic plane problems [9]. Through combining constant element of DDM and FSM,
67 Wong *et al.* developed a set of open-source codes to simulate 3D cracks [18]. Rezvan *et al.* extended
68 DDM to 3D analysis and modelled fatigue crack growth of brittle materials [19]. Although the
69 constant element method is more widely used in general engineering applications, the linear
70 element, higher-order element, some special element [20], and including the isogeometric BEM
71 [21] had been essentially developed to improve the accuracy of calculation at the same number of
72 elements as well as the same boundary discretization. Considering the continuity of sought
73 unknown variables being distributed across neighboring elements as well as the computational
74 efficiency in the numerical solution to inverse problems, based on Crouch's constant element
75 program, the source code for two-node linear element of boundary element method was developed.

76 The forwarding analysis of boundary value problems in engineering mostly refers to
77 establishing the governing equation from boundary loading as source senders and to solve
78 displacement, stress and strain at objective receivers through the constitutive relationship of rock
79 mass under the premise of known properties. In contrasted with a forwarding problem, an inverse
80 problem is to measure the responses to backwardly calculate their causes. The latter can usually
81 not be directly monitored or explicitly represented by the forwarding problem [22,23]. The solution
82 to governing equations of inverse problem always falls into ill-posed. When the number of
83 equations is less than that of unknowns, the coefficient matrix is rank deficient and the problem is
84 called rank deficient problem. While the number of characteristic values of coefficient matrix is
85 larger than that of unknown variable or the error of calculation or measured sample data are enough

large, solution to the equations will change dramatically and lose its continuity between neighboring elements, which is called ill-posed problem [24]. The calculation methods of inverse problems mainly include regularization methods, optimization methods, statistical methods, etc. [25]. Regularization method is very effective in treating ill-posed problems. Variational regularization method proposed by Tikhonov [26], iterative regularization method put forward by Landweber [27], and spatial regularization method founded by Zabaras [28], all of these can be used to deal with the ill-posed problem for inverse problems. With the continuous development of inverse problem theory and the increasingly maturity of numerical methods, it is a natural demand from practice that solution to inverse problems using numerical modelling should be applied to analyze engineering process. Maniatty *et al.* adopted diagonal regularization method to solve unknown stress boundary conditions with the help of finite element method [23]. Schnur *et al.* combined spatial regularization with boundary element method to solve boundary pressure with analytical solution [29]. Zhang *et al.* used constrained least squares optimization method to reversely calculate residual stress and contact stress [30]. Combined with numerical modelling and solutions, the application scopes of inverse problem in engineering will be greatly extended, and the approximating accuracy in complicated shape of modelling will be also improved significantly through the corresponding boundary element method development.

In view of interpreted surface displacements or observative borehole deformations caused by a hydraulic fracturing implementation, the commonly adopted monitoring methods mainly include Global Positioning System (GPS), Interferometric Synthetic Aperture Radar (InSAR), inclinometer, etc. [31]. GPS method is used to monitor the development of small or hidden fissures in the ground vegetation, but repeated surveys are required to exclude weather and climate influence [32]. InSAR

is a method that two or more synthetic aperture radar images are used to calculate small changes out of original topographic and geomorphic surface of the target area by utilizing wave phase differences through returning way from satellites, but it may be interfered by local atmospheric and geographical conditions [33]. The inclinometer, which is installed in the shallow buried depth of the ground and has been applied commercially, can monitor extremely small deformation with high sensitivity and has the advantages of high precision, well stability and remote real-time continuous measurement [34].

A two-dimensional linear element of BEM code and an inverse solution strategy were developed to invert the fluid pressure in reservoir from its induced surface displacements. The development and verification of solving process of the plane problems laid a solid foundation for the upcoming 3D analysis and application. The numerical solution work-flow of inverse problem was based on the independent development of linear element boundary element. In this paper, the combination between developing linear element BEM source code program and implementing numerical solution to inverse problem were pursued. Its application was demonstrated when the equivalent loads applied onto the walls of a reopened discontinuity during reservoir fracturing stimulation underground. The loads can be figured out from the induced minute displacements of ground surface which were monitored by tiltmeter array.

2. Development of linear element type of BEM for analyzing plane elastic problems

2.1 Setting up the boundary integral equations with regard to linear element

The indirect BEM includes Fictitious Stress Method (FSM) and Displacement Discontinuity Method (DDM). On the basis of constant-element BEM code, a linear-element BEM code called

LE-BEM ver. 1.0 was developed using DDM at this stage.

The DDM is that on the basis of establishing the matrix of influence factors among which each element A_{ij} represents the response with regards to element j being caused by a unit load or a unit dislocation constantly distributed along boundary element *i*. Due to the principle of superposition is applicable to linear elastic problems, as the unknown variables a group of linear combination of fictitious loads or displacement discontinuities can be regarded as intermediate multiplicators are to be solved so as to satisfy the known boundary conditions. After the intermediate displacement discontinuities being sought, their linear combination can function to figure out the response at any arbitrary position within the domain because they are the elemental integral of the fundamental solution which depend on the coordinates.

The normal and the shearing displacement discontinuities (DDs), i.e. D_x, and D_y, at the origin O (0,0) of Cartesian coordinate system [35] are defined as:

$$\begin{aligned} D_{\overline{x}}(\overline{x},0) &= u_{\overline{x}}(\overline{x},0_-) - u_{\overline{x}}(\overline{x},0_+) \\ D_{\overline{y}}(\overline{x},0) &= u_{\overline{y}}(\overline{x},0_-) - u_{\overline{y}}(\overline{x},0_+) \end{aligned} \tag{1}$$

where, $u_i(i = x, y)$ is the relative displacement between the two walls of an infinitely short fracture. Mathematically speaking, they are the displacement discrepancy of an infinitesimal long crack which undergoes vertical separation or overlapping and horizontal dislocation, respectively. The displacement and stress at point P (*x, y*) due to the DDs at the origin are formulated as:

$$\begin{aligned} u_x &= D_x\left[2(1-v)g_{,y} - yg_{,xx}\right] + D_y\left[-(1-2v)g_{,x} - yg_{,xy}\right] \\ u_y &= D_x\left[(1-2v)g_{,x} - yg_{,xy}\right] + D_y\left[2(1-v)g_{,y} - yg_{,yy}\right] \\ \sigma_{xx} &= 2GD_x\left[2g_{,xy} - yg_{,xxx}\right] + 2GD_y\left[g_{,yy} - yg_{,xxy}\right] \\ \sigma_{yy} &= 2GD_x\left[-yg_{,xyy}\right] + 2GD_y\left[g_{,yy} - yg_{,yyy}\right] \\ \sigma_{xy} &= 2GD_x\left[g_{,yy} - yg_{,xxy}\right] + 2GD_y\left[-yg_{,xyy}\right] \end{aligned} \tag{2}$$

where, D_x and D_y are the tangent and normal discontinuous displacement discontinuity variables,

148 respectively. G is the shearing modulus; v is the Poisson's ratio; g is expressed as:

149 $$g(x,y) = -1/\big(4\pi(1-v)\big)\ln(x^2+y^2)^{1/2} \tag{3}$$

150 and g_i, g_{ij}, g_{ijk} ($i, j, k = x, y$) denote the first-, second- and third-order partial derivatives of g with
151 respect to the subscripts, respectively. The linear distribution of displacement discontinuities along
152 one boundary element needs to be determined by two nodes. As shown in Fig. 1, since two adjacent
153 elements share one common endpoint, in order to avoid singularity of the integration at each
154 elemental endpoint, the nodes of a linear element are chosen as at the position of 1/4 elemental
155 length inward away from the two endpoints, being numbered as x_{2k-1} and x_{2k} ($k = 1,2 \ldots N$， where,
156 N is the total number of elements). For displacement discontinuity DDs on each element, the linear
157 distribution can be expressed as:

158 $$\begin{aligned} D_i &= N_1 D_i^1 + N_2 D_i^2 \\ N_1 &= \big(\xi - x_{j+1}\big)/\big(x_j - x_{j+1}\big) \\ N_2 &= \big(\xi - x_j\big)/\big(x_{j+1} - x_j\big) \end{aligned} \tag{4}$$

159 where, D_i^1 and D_i^2 $(i = x,\ y)$are multiplicator shown in Fig. 1. N_1 and N_2 are shape functions; x_j
160 and x_{j+1} are the two endpoints of the element, respectively; $\xi \in [x_j,\ x_{j+1}]$。

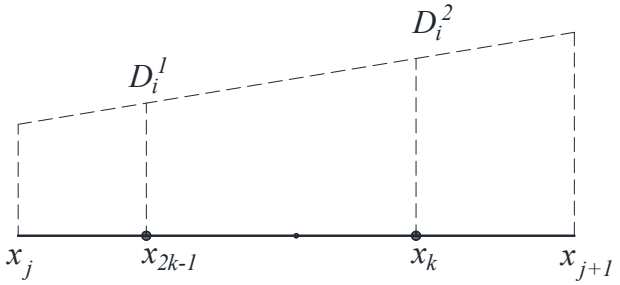

161

162 Fig. 1 Positioning of two nodes and their displacement discontinuities (D_x, D_y) of a linear element

163 For the distribution of displacement discontinuities over a linear element, the corresponding

induced displacements and stresses can be in a close-form way expressed ed by simply substituting the following *f* for *g* in Eq. (2), where, *f* is the Kernel function manifesting as integral of the linear distribution of *g* over an element, given by:

$$\begin{aligned} \mathrm{f}(x,y) &= \int_{x_i}^{x_{i+1}} \mathrm{D}_i * g(x-\xi,y)d\xi \\ &= \int_{x_i}^{x_{i+1}} N_1 D_i^1 * g(x-\xi,y)d\xi + \int_{x_i}^{x_{i+1}} N_2 D_i^2 * g(x-\xi,y)d\xi \\ &= D_i^1 * f_1(x,y) + D_i^2 * f_2(x,y) \end{aligned} \tag{5}$$

For odd-numbered nodes(x_{2i-1}), x_j and x_{j+1} are values of -1/2a and 3/2a, respectively, where, a is the half length of an element. For even-numbered nodes(x_{2i}), x_j and x_{j+1} are values of -3/2a and 1/2a, respectively. Integral results of $f_1(x,y)$ and $f_2(x,y)$ parts are as shown in Appendix A1.

Therefore, in term of an elemental source, its induced displacements and stresses at any point P (x, y) within the plane can be expressed as:

$$\begin{aligned} u_x &= D_x^1\left[2(1-v)f_{1,y} - yf_{1,xx}\right] + D_y^1\left[-(1-2v)f_{1,x} - yf_{1,xy}\right] \\ &\quad + D_x^2\left[2(1-v)f_{2,y} - yf_{2,xx}\right] + D_y^2\left[-(1-2v)f_{2,x} - yf_{2,xy}\right] \\ u_y &= D_x^1\left[(1-2v)f_{1,x} - yf_{1,xy}\right] + D_y^1\left[2(1-v)f_{1,y} - yf_{1,yy}\right] \\ &\quad + D_x^2\left[(1-2v)f_{2,x} - yf_{2,xy}\right] + D_y^2\left[2(1-v)f_{2,y} - yf_{2,yy}\right] \\ \sigma_{xx} &= 2GD_x^1\left[+2f_{1,xy} + yf_{1,xyy}\right] + 2GD_y^1\left[f_{1,yy} + yf_{1,yyy}\right] \\ &\quad + 2GD_x^2\left[+2f_{2,xy} + yf_{2,xyy}\right] + 2GD_y^2\left[f_{2,yy} + yf_{2,yyy}\right] \\ \sigma_{yy} &= 2GD_x^1\left[-yf_{1,xyy}\right] + 2GD_y^1\left[f_{1,yy} - yf_{1,yyy}\right] \\ &\quad + 2GD_x^2\left[+2f_{2,xy} + yf_{2,xyy}\right] + 2GD_y^2\left[f_{2,yy} + yf_{2,yyy}\right] \\ \sigma_{xy} &= 2GD_x^1\left[f_{1,yy} + yf_{1,yyy}\right] + 2GD_y^1\left[-yf_{1,xyy}\right] \\ &\quad + 2GD_x^2\left[f_{2,yy} + yf_{2,yyy}\right] + 2GD_y^2\left[-yf_{2,xyy}\right] \end{aligned} \tag{6}$$

The derivatives of $f_1(x,y)$ and $f_2(x,y)$ are all derived from the linear integration of the corresponding derivatives of $g(x,y)$ [9] according to Eq. (5). Their integration results are shown in Appendix A1.

Assuming that the boundary is discretized into *N* elements, the induced displacements and stresses of the *i*th element at its nodes can be calculated by superimposed individual contributions

of *j*th elements, namely:

$$\begin{aligned} \overset{i}{u}_x &= \sum_{j=1}^{N} \overset{ij}{U}_{xx} \overset{j}{D}_x^1 + \sum_{j=1}^{N} \overset{ij}{U}_{xy} \overset{j}{D}_y^1 + \sum_{j=1}^{N} \overset{ij}{U}_{xx} \overset{j}{D}_x^2 + \sum_{j=1}^{N} \overset{ij}{U}_{xy} \overset{j}{D}_y^2 \\ \overset{i}{u}_y &= \sum_{j=1}^{N} \overset{ij}{U}_{yx} \overset{j}{D}_x^1 + \sum_{j=1}^{N} \overset{ij}{U}_{yy} \overset{j}{D}_y^1 + \sum_{j=1}^{N} \overset{ij}{U}_{yx} \overset{j}{D}_x^2 + \sum_{j=1}^{N} \overset{ij}{U}_{yy} \overset{j}{D}_y^2 \end{aligned} \tag{7}$$

$$\begin{aligned} \sigma_{xx} &= \sum_{j=1}^{N} \overset{ij}{S}_{xxx} \overset{j}{D}_x^1 + \sum_{j=1}^{N} \overset{ij}{S}_{xxy} \overset{j}{D}_y^1 + \sum_{j=1}^{N} \overset{ij}{S}_{xxx} \overset{j}{D}_x^2 + \sum_{j=1}^{N} \overset{ij}{S}_{xxy} \overset{j}{D}_y^2 \\ \sigma_{yy} &= \sum_{j=1}^{N} \overset{ij}{S}_{yyx} \overset{j}{D}_x^1 + \sum_{j=1}^{N} \overset{ij}{S}_{yyy} \overset{j}{D}_y^1 + \sum_{j=1}^{N} \overset{ij}{S}_{yyx} \overset{j}{D}_x^2 + \sum_{j=1}^{N} \overset{ij}{S}_{yyy} \overset{j}{D}_y^2 \\ \sigma_{xy} &= \sum_{j=1}^{N} \overset{ij}{S}_{xyx} \overset{j}{D}_x^1 + \sum_{j=1}^{N} \overset{ij}{S}_{xyy} \overset{j}{D}_y^1 + \sum_{j=1}^{N} \overset{ij}{S}_{xyx} \overset{j}{D}_x^2 + \sum_{j=1}^{N} \overset{ij}{S}_{xyy} \overset{j}{D}_y^2 \end{aligned} \tag{8}$$

where, U_{ij} and S_{ijk} (*i, j, k=x, y*) are termed the influence coefficients, which can be calculated by substituting *f* for *g* in Eq. (6) and performing coordinate transformations. The assembles of U_{ij} and S_{ijk} form the influence coefficient matrix [U] and [S], so Eq. (7) and Eq. (8) can be written as follows:

$$u = [U][D] \tag{9}$$

$$\sigma = [S][D] \tag{10}$$

Eq. (9) and Eq. (10) are the final linear equations for solving DDs. DDs on the boundary can be obtained by solving the equation, then the stress and displacements at any point in the domain can be obtained.

2.2 Verification of the linear element of boundary element method program

The validity of the algorithm and program was verified by considering the opening quantity and tip stress of the crack in infinite body. There exists a linear crack with its length 2*b* under pressure *P* in an infinite body, with zero stresses and displacements at infinity, the Young's modulus *E* and Poisson's ratio *v*. The problem is defined as follows

$$\begin{aligned} \sigma_{xy} &= 0 \qquad -\infty < x < \infty, y = 0 \\ \sigma_{yy} &= -p \qquad |x| < b, y = 0 \\ u_y &= 0 \qquad |x| \geq b, y = 0 \end{aligned} \tag{11}$$

The analytical solution of the crack opening quantity is

$$\hat{u}_y(x) = u_y(x, 0_-) - u_y(x, 0_+) = -4(1-v^2)pb(1-x^2/b^2)^{1/2}/E \tag{12}$$

this equation is known as the Snedden's solution [35].

Used the self-developed LE-BEM code to calculate the opening quantity of a 4 m long but internally pressured by 100kPa crack that is within plane infinite elastic media with Poisson's ratio 0.1 and Young's modulus 200 MPa. The crack was separated into 50 linear elements along the length direction, that compared with the constant element code with 50 and 250 elements [9] and the Snedden's solution. The results of the linear element program were closer to the analytical solution, and the calculation accuracy was increased by 5 times nearly in Fig. 2.

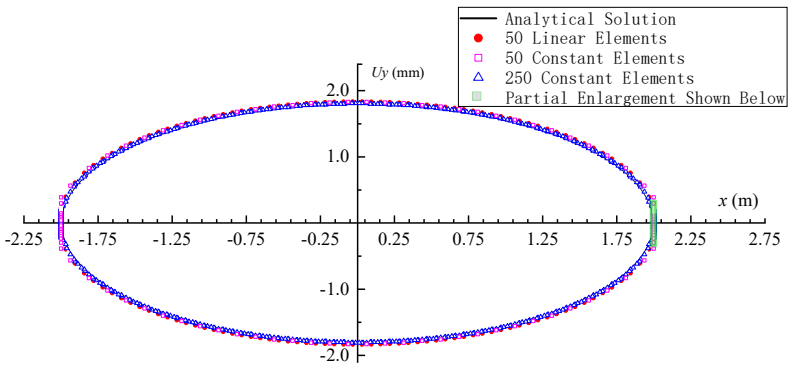

(a) The aperture of an opening crack simulated by different methods

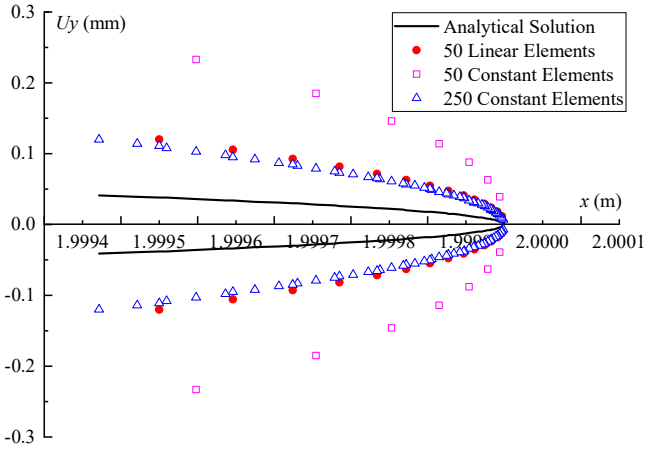

(b) Enlarged view of a portion

Fig. 2 The normal displacements of an innerly pressured crack within a plane infinite elastic media

The stresses in vicinity of crack-tip were verified by analytical solution and constant element type of BEM code. In order to further verify the accuracy of LE-BEM code, the computational results with the same numbers of divisions were compared between the linear element program and constant-element program.

A certain inner pressure loaded onto the walls cause the opening of a crack, which belonged to fracture type I. The analytical solution was shown in the following equation [36], the formula applied for $r \ll 2b$. The polar coordinates with the crack tip as their origin were introduced, as shown in Fig. 3. For the fracture type I, σ_{yy} is the most remarkably concerned stress component, so we analyzed the values of σ_{yy} when $\theta = 0^{\circ}$ and $\theta = 90^{\circ}$.

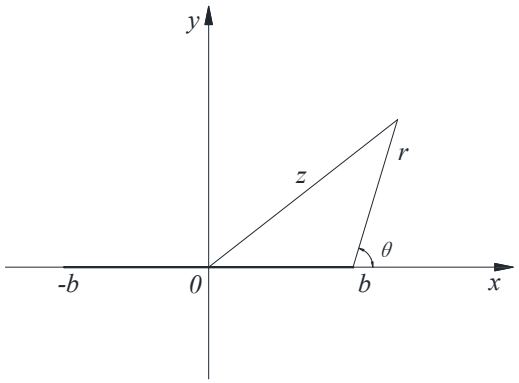

Fig. 3 The polar coordinates (r, θ) originating from right crack tip

$$\sigma_{yy} = \frac{K_I}{\sqrt{2\pi}} \cos\frac{\theta}{2}\left(1 + \sin\frac{\theta}{2}\sin\frac{3\theta}{2}\right) \tag{13}$$

where, $K_I = P\sqrt{\pi b}$.

In order to compute the stress in vicinity of the crack tip, i.e., r≪2b, the boundary has been refined. As shown in Fig. 4, the simulated results of the LE-BEM code were consistent with the tendency of magnitudes with regarding to the analytical solution and the simulated results of the constant-element code, which proved that the developed source code was correct. The closer it was to the crack tip, the closer the calculation result of the linear element was to the analytical solution, which proved that the calculation accuracy of the linear element was higher near the crack tip than that of the constant-element code. As the distance from the tip get farther and farther, the results of LE-BEM code were closer to those of the analytical solution.

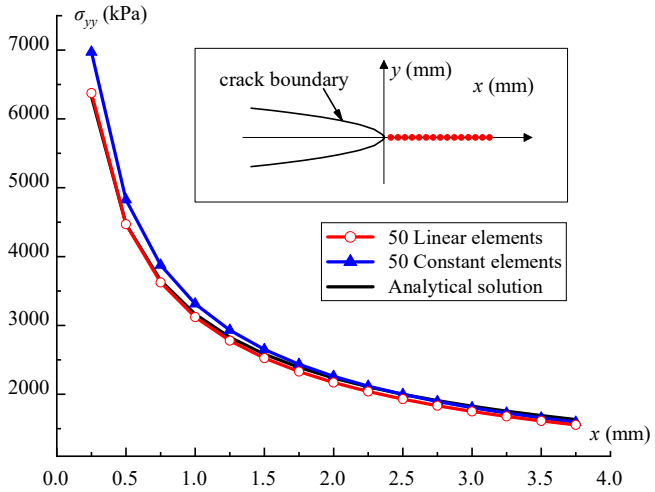

(a) σ_{yy} in vicinity of crack tip along the x axis

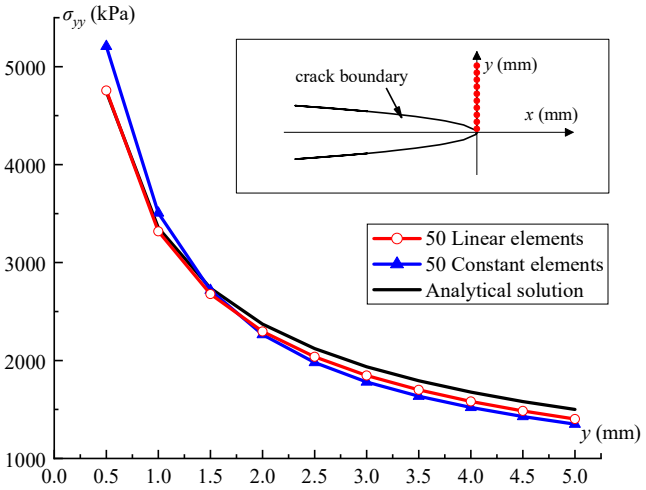

(b) σ_{yy} in vicinity of crack tip along the y axis

Fig. 4 Comparison of vertical normal stress in vicinity of crack tip computed by different methods

3 Numerical solution to inverse problem

3.1 Mathematical definition of linear elastic inverse problem

The boundary of the isotropic homogeneous elastic domain B is indicated as ∂B. The inverse problem is expressed by tensors as follows

$$
\begin{aligned}
&\sigma_{ij,j} = 0 && (a)\\
&\sigma_{ij} = \frac{Ev}{(1+v)(1-2v)}\varepsilon_{kk}\delta_{ij} + \frac{E}{(1+v)}\varepsilon_{ij} && (b)\\
&\varepsilon_{ij} = \frac{1}{2}\left(u_{i,j} + u_{j,i}\right) && (c)\\
&u_i(\bar{x}_k) \cong \hat{u}_i^k,\ \bar{x}_k \in (B - \partial B),\ k = 1, \dots, N && (d)\\
&\tau_i(\bar{x}) \cong \hat{\tau}_i(\bar{x}),\ \bar{x} \in \partial B_{i1} && (e)\\
&u_i(\bar{x}) \cong \hat{u}_i^B(\bar{x}),\ \bar{x} \in \partial B_{i2} && (f)
\end{aligned}
\tag{14}
$$

where, *i, j=1, 2*; E is Young's modulus; v is Poisson's ratio. Equations (a), (b), (c) are equilibrium differential equations, physical equations, and geometrical equations, respectively. Equation (d) represents the measured displacements at the monitoring points. Equations (e) and (f) are known stress type and known displacement type boundary conditions, respectively. The rest of the unknown boundary conditions $\partial \mathrm{B_{i3}}$（$\partial \mathrm{B_{i3}} = \partial \mathrm{B_i} - \partial \mathrm{B_{i1}} - \partial \mathrm{B_{i2}}$）can be solved by the inverse problem.

The inverse problem equations in engineering are often rank deficit and ill-posed. By means of space regularization, ill-posed problem is transformed into well-posed problem to find the approximate solution, and then the stable solution of the equation will be obtained.

3.2 Space regularization method

In order to solve the inverse elasticity problem for tractions, the boundary is divided into M straight line segments, and the stress at any point can be taken as the response caused by the displacement on the boundary elements as follows

$$\{F\} = \{K\}\{u\} \tag{15}$$

where, $\{F\}$ is the vector of nodal forces applied on the boundary, $\{K\}$ is the matrix of influence coefficients, $\{u\}$ is the vector of nodal displacement. In the forward problem, $\{F\}$ is known and $\{u\}$ can be calculated by Equation 15. In the inverse problem, the vector $\{\tau^*\}$ is unknown, which is

related to the displacement $\{u_{in}\}$ of the sensor position and the sensitivity matrix $\{S\}$, the equation is reconstructed as

$$\{u_{in}\} = \{S\}\{\tau^*\} \tag{16}$$

The sensitivity matrix $\{S\}$ is the displacement component caused by the unit change in each traction component at each sensor position. To calculate $\{S\}$, a unit stress variable is applied to the traction boundary elements once at a time while keeping the remaining boundary's tractions zero, and Equation 15 is used repeatedly to solve the displacements at the sensor positions.

To determine the $\{\tau^*\}$, minimizing the error between the calculated displacements $\{u_{in}\}$ and the experimentally measured displacements $\{\hat{u}\}$ needs to be solved as follows

$$\min_{\{\tau^*\}} E = \min_{\{\tau^*\}} \frac{1}{2}(\{u_{in}\} - \{\hat{u}\})^T(\{u_{in}\} - \{\hat{u}\}) \tag{17}$$

In order to solve the ill-posed problem of the coefficient matrix, the constraint of minimizing R is introduced:

$$R = \frac{1}{2}\alpha_0^1 \int_{\partial B_{13}} (\tau_x)^2 \, ds + \frac{1}{2}\alpha_1^1 \int_{\partial B_{13}} \left(\frac{\tau_x}{\partial s}\right)^2 ds + \frac{1}{2}\alpha_0^1 \int_{\partial B_{13}} (\tau_y)^2 \, ds + \frac{1}{2}\alpha_1^1 \int_{\partial B_{13}} \left(\frac{\tau_y}{\partial s}\right)^2 ds \tag{18}$$

The above Equation defines the first-order regularization of the unknown stress condition, where the regularization parameters α_0^i and α_1^i(i=1,2) control the type and degree of the continuity and smoothness, which should be able to eliminate the singularity of the problem without affecting the least squares solution. The relative size of equation system can be selected by referring to the existing measured data. Parts 1 and 2 of Equation (18) will make the change rates of τ_x and τ_x tending to 0, and parts 3 and 4 will make the change rates of τ_y and τ_y tending to 0. Strive for the partial derivatives of $\{\tau^*\}$ after adding Equation (18) into Equation (17). When the partial

derivative is equal to 0, the calculation expression about $\{\tau^*\}$ is obtained as

$$([S]^T[S] + [F])\{\tau^*\} = [S]^T\{\hat{u}\} \tag{19}$$

where,

$$[F] = \begin{bmatrix} \alpha_0^1[F_0] + \alpha_1^1[F_1] & [0] \\ [0] & \alpha_0^2[F_0'] + \alpha_1^2[F_1'] \end{bmatrix} \tag{20}$$

$[F_0]$ and $[F_1]$ are zero- and first-order regularization terms defined on ∂B_{13} (∂B_{13} were divided into J_1 linear units of length of ΔS_i), $[F_0']$ and $[F_1']$ are expressions similar to (21) and (22) defined on ∂B_{23}.

$$[F_0] = \begin{bmatrix} \frac{\Delta S_1}{3} & \frac{\Delta S_1}{6} & & \\ \frac{\Delta S_1}{6} & \frac{\Delta S_1}{3} + \frac{\Delta S_2}{3} & \frac{\Delta S_2}{6} & \\ & \cdots \quad \cdots & \cdots & \cdots \\ & & \frac{\Delta S_{J1}}{6} & \frac{\Delta S_{J1}}{3} \end{bmatrix} \tag{21}$$

$$[F_1] = \begin{bmatrix} \frac{1}{\Delta S_1} & -\frac{1}{\Delta S_1} & & \\ -\frac{1}{\Delta S_1} & \frac{1}{\Delta S_1} + \frac{1}{\Delta S_2} & -\frac{1}{\Delta S_2} & \\ & \cdots \quad \cdots & \cdots & \cdots \\ & & -\frac{1}{\Delta S_{J1}} & \frac{1}{\Delta S_{J1}} \end{bmatrix} \tag{22}$$

This equation can be used to transform the primitive mathematical definition of inverse problem into a well-posed one.

4 Verification through a computational example

As shown in Fig. 5, a square thin plate with a centered square hole is an elastic body whose top is loaded by linearly distributed pressures symmetrical by the middle line. The self-developed LE-BEM code was used to carry out forward modeling to calculate the displacements at the monitoring points, which was taken as the known condition being used to calculate the boundary

stress by inversion program. The correctness and precision of the self-developed LE-BEM code were proved compared to the calculation results of constant element BEM code.

4.1 Forwarding simulation using linear element of boundary element method

The 2D model for a 20 m×20 m size of media with a 2 m×2 m square hole at the center is established. The elastic media is with its Young's modulus E=3.0×10^4 kPa and Poisson's ratio v=0.3. As shown in Fig. 5, the load was applied on the model top. Nine sensors are set at the positions of x=-8 m, -6 m, -4 m, -2 m, 0 m, 2 m, 4 m, 6 m, 8 m and y=9, successively. The upper boundary and the square hole boundaries were discretized into 20 and 40 elements, respectively.

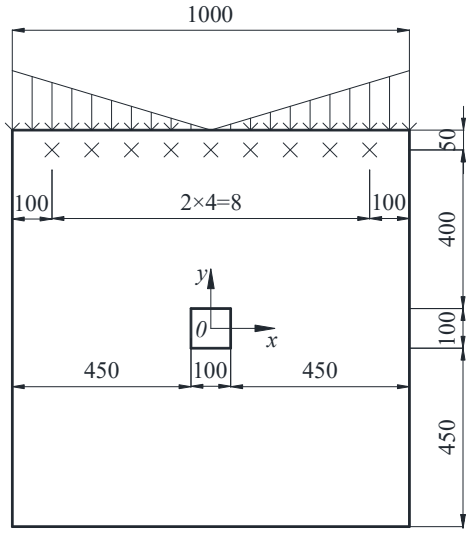

Fig. 5 The model geometry (unit: m) and loading condition (Max: 100 kPa)

The forward numerical simulation was carried out using the linear and constant element of boundary element programs, respectively. The boundaries for constant element program modelling were discretized as both the same and 5 times as those for the linear element. The displacements of monitoring points (x=0 m, 2 m, 4 m, 6 m, 8 m and y=9) were listed in Tab. 1.

Tab. 1 Displacements at the sensors

Sensor positions x/m	Linear elements		Constant elements		5 times constant elements	
	U_x/mm	U_y/mm	U_x/mm	U_y/mm	U_x/mm	U_y/mm
0	0	-5.42	0	-5.41	0	-5.44
2	1.98	-7.09	1.88	-7.09	1.89	-7.10
4	3.91	-10.73	3.88	-10.74	3.90	-10.73
6	5.94	-15.11	5.88	-15.13	5.92	-15.10
8	8.04	-19.59	7.95	-19.59	8.02	-19.51

The figure showed that the result of the linear element code was between the two discrete cases of the constant element code, which indicated that the linear element program was correct and with higher accuracy than the constant element program with the same discretization. Then, the linear element program was used for looping simulation to obtain the $\{S\}$ matrix of the inverse problem, which will lay the foundation to solve the inverse problem.

4.2 Numerical solution to inverse problem

The displacements of the monitoring points and the $\{S\}$ matrix obtained built from successively but loop-wisely calling the linear element code were input into the inverse problem program to solve the loads on the boundary $\partial \mathrm{B}_{13}$. In order to ensure the stability and accuracy of solution, different regularization parameters α_0^i and $\alpha_1^i (i = 1, 2)$ were selected, their corresponding results were shown in Fig. 6. It can be seen that the results are acceptably stable and accurate with little number of monitoring points, and the regularization parameters impact the stability of the solution significantly. When $\alpha_0^i = 10^{-18}$, $\alpha_1^i = 10^{-15} (i = 1,2)$ the stability and

accuracy of the obtained solution are the best among these three choices.

The influence of monitoring error on inversion results was discussed. Fig. 7 showed the inversion results of the top boundary normal forces under different monitoring errors. The results manifest that in the presence of 5% measurement error, the inversion results were still stable relatively which are not much different from the accurate measurement results, indicating that this method was anti-interference to measurement errors, and adaptable to keep robust from unavoidable measurement errors in practical applications.

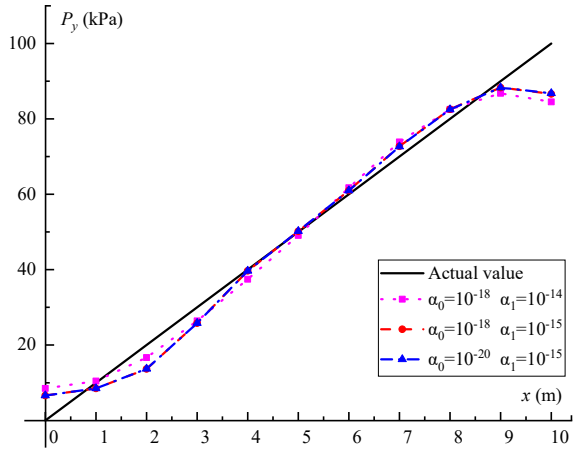

Fig. 6 The loads on the top modelled by inverse solution corresponding to different regularization parameters

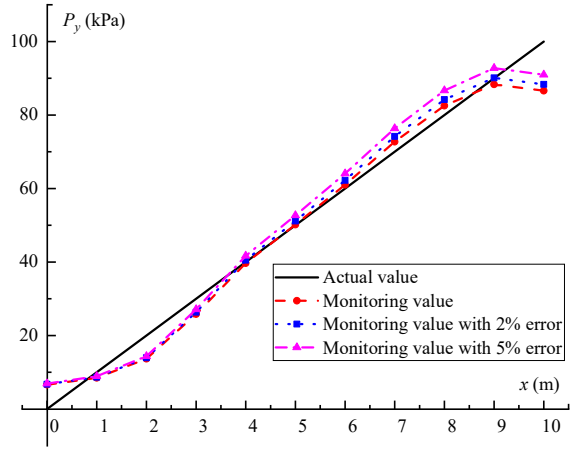

Fig. 7 The loads on the top modelled by inverse solution corresponding to different monitoring deviations

In general, even with a small number of monitoring points, a stable and accuracy solution can also be obtained inversely using spatial regularization. Meanwhile, this method has a certain immunity from the inaccuracy of monitoring data, which implies the inverse problem numerical solution will be robustly further applicable in the engineering.

5 An application example during a field project

Tiltmeters are widely used in reservoirs sensitive to small deforming tilting angles with nanometer radian precision. It can monitor not only the deformation on ground surface, but also that along wellbore. In the latter case, the tiltmeter array is placed inside the well. During the fracturing implementation to stimulate a relatively shallow coal seam in Alberta, Canada, a tiltmeter array was installed on the surface near the injection well, as shown in Fig. 8. The position and shape of the fracture were determined by analyzing the monitoring data during the stable re-opening stage. By analyzing the monitoring data of the surface tiltmeters, it can be seen that the surface displacement caused by fracturing of the reservoir exhibits as a hump-like shape, and the maximum displacement was interpreted as 0.049 mm, as shown in Fig. 9.

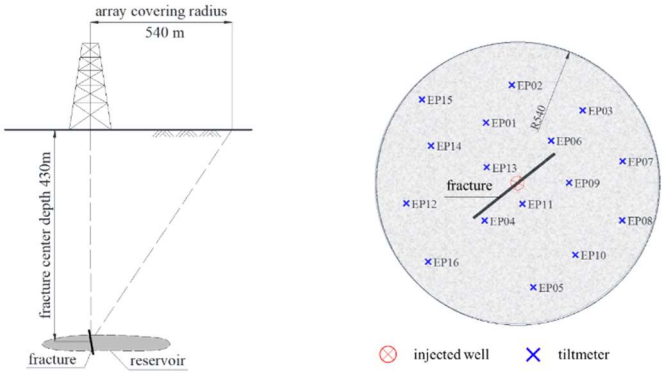

(a) Sectional view (b) Floor plane

Fig. 8 Schematic diagram of the surface installation of tiltmeter array

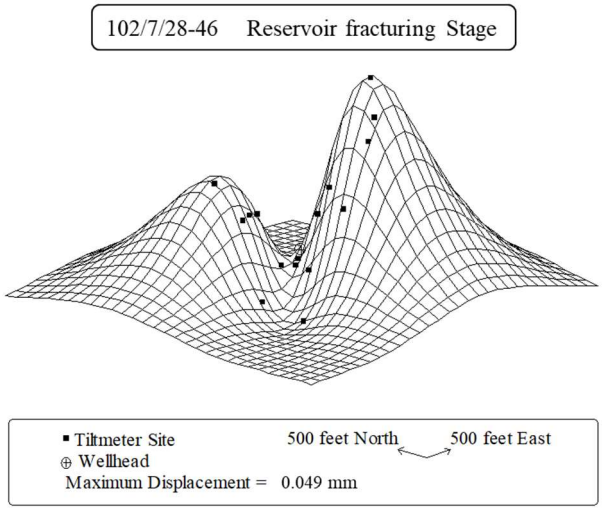

Fig. 9 The tiltmeter array monitored surface displacements

5.1 Forward model to simulate surface deformation

The fracture was caused to open by a net pressure, which yields by subtracting the initial minimum principal stress from the fluid pressure on the fracture wall, resulting in the surface deformation.

This process is simplified to apply a uniform pressure to a strip-shaped crack inside a half infinite elastic media, and simulate the induced surface deformation in a forwarding way, in order to fit the deformation data monitored by the tiltmeter array. The assumptions had been adopted in the calculation process as follows:

(1) The formations were assumed to be a unified homogeneous isotropic elastic continuum with its average Young's modulus and Poisson's ratio.

(2) The length of the crack about 300 m was much larger than the height about 40 m and centimeter-grade opening, which roughly conformed to plane-strain problem hypothesis. Therefore, the cross-section with the largest surface displacement was selected to establish the plane model

corresponding to the high-width cross-section of the crack.

(3) Considering that the liquid injection process time was short and the injection amount was large, the portion of the liquid percolating out of the crack walls and into the surroundings would be neglected, and the pore pressure acting on crack deformation were simplified as a process of applying quasi-static loading on the fracture walls.

As shown in Fig. 10, the LE-BEM code was used to simulate vertical fracture with an inclination angle of 86°. The fracture at depth with the length of 40 m was divided into 60 elements, in which the first and last elements are tip elements [37], and the rest are linear elements. The surface boundary simulated by an enough long crack with the length of 2000 m and a free boundary was divided into 400 elements to ensure the calculation accuracy. The model parameters used in the numerical simulation are shown in Tab. 2, and the surface deformation results calculated by the numerical simulation are shown in Fig. 11.

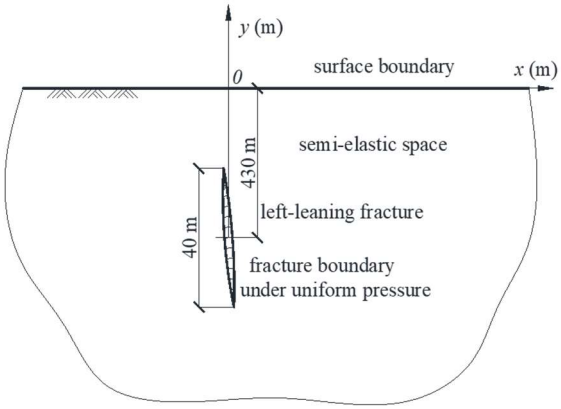

Fig. 10 The model for a pressured deep fracture inducing ground minute displacements

383 Tab. 2 Model parameters

Parameter Type	Unit	Quantity
Length of surface boundary	m	2000
Depth of crack top	m	410
Depth of crack bottom	m	450
Crack inclination	º	86
Average Young's modulus	GPa	25
Average Poisson's ratio	-	0.25
Net pressure of fracturing	MPa	3.5

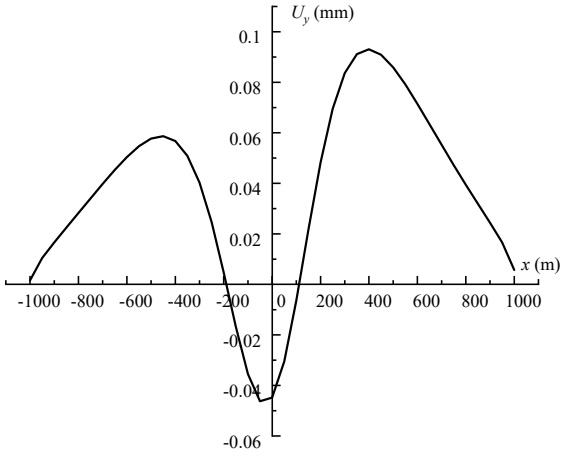

384

385 Fig. 11 Simulation results of surface deformation caused by a fracture

386 The surface displacements calculated by the LE-BEM code were roughly consistent with the
387 surface displacements obtained according to the tiltmeter array monitored data interpretation, that
388 shown double-hump shape, and the left and right peak values were different. The maximum surface
389 uplift displacement obtained by the linear elements program was 0.093 mm, which was larger than
390 the measured data 0.049 mm. Since the model adopted the assumption of plane strain, and the range

of fracture length and fracture net pressure in the third direction of the actual project might not be connected, the calculation result was larger. However, the deformation morphology is consistent with the actual monitoring results, and the value is in the same order of magnitude, which proves the correctness of the results.

5.2 Influence of fracture dip on induced surface deformation

In order to analyze the influence of fracture dip angle on surface deformation, the surface deformation was simulated by changing only fracture dip angle and keeping other parameters unchanged. The model size, unit division, pressure and boundary conditions were the same as those in section 5.1. Only the fracture inclination angles were changed, which were 0º and 274º respectively, as shown in Fig. 12.

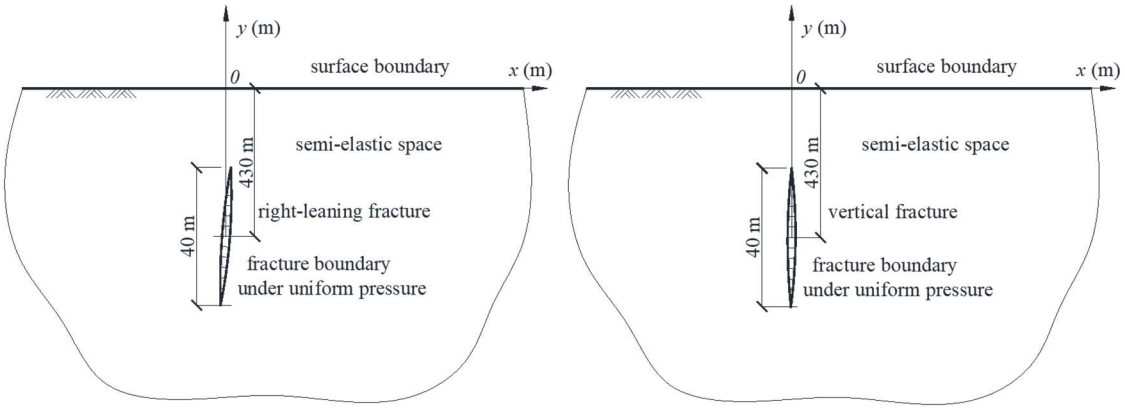

Fig. 12 Different leaning fracture models

The results shown that when the fracture was vertical, the surface deformation was hump symmetrically. When the fracture inclined to the right, the left hump was higher than the right hump, as shown in Fig. 13. The reason for this phenomenon was that: the strain caused by ground stress on the upper side of the fracture was directly transmitted to the surface, while part of the strain on

the lower side of the fracture was transmitted to the deep, so the upward transmission as dispersed, showing the phenomenon of unequal peak values of the humps on both sides. While in vertical fractures, the pressure transfers were the same on the left and right sides, so the humps on the surface were symmetrical. The results showed that the oblique reservoir fracture affected the trend of formation deformation.

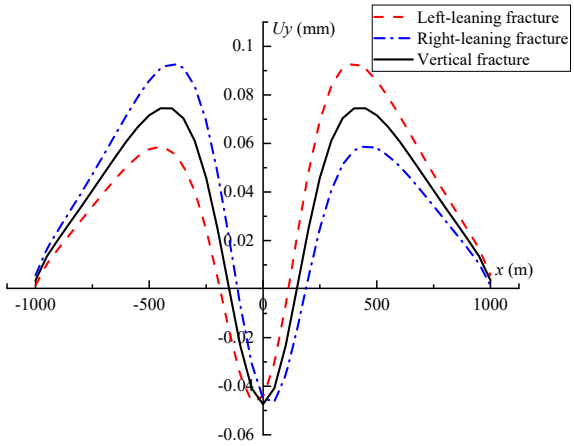

Fig. 13 Surface deformations caused by fractures with different inclinations

5.3 Inverse solution to the net pressure onto fracture walls

Taking the surface just above the fracture center as the coordinate origin, a line of monitoring points was arranged on the surface. 15 monitoring points with the depth of 5 meters below the surface were arranged within a radius of 500 meters around the injected well. Considering that the closer to the fracture horizontal position, the more obvious the corresponding deformation for the ground surface. Within the radius of 200 meters, a monitoring point was set every 50 meters, and within the radius of 200-500 meters, a monitoring point was set every 100 meter, with a total of 15 monitoring points. Fig. 14 shows half of the monitoring diagram.

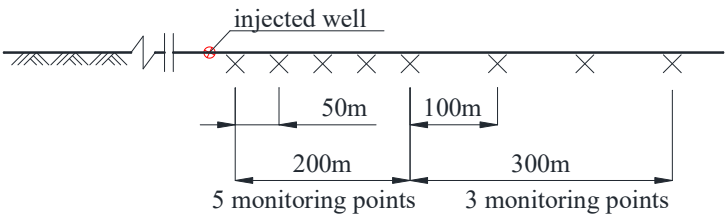

Fig. 14 The layout of monitoring points

Taking the displacement of the monitoring point as the known information, the LE-BEM code was cyclically called to obtain the $\{S\}$ matrix, which was used as the input condition of the inverse problem program. The regularization parameters were adjusted to solve the inverse problem, and the normal pressure at the fracture was obtained as shown in Fig. 15.

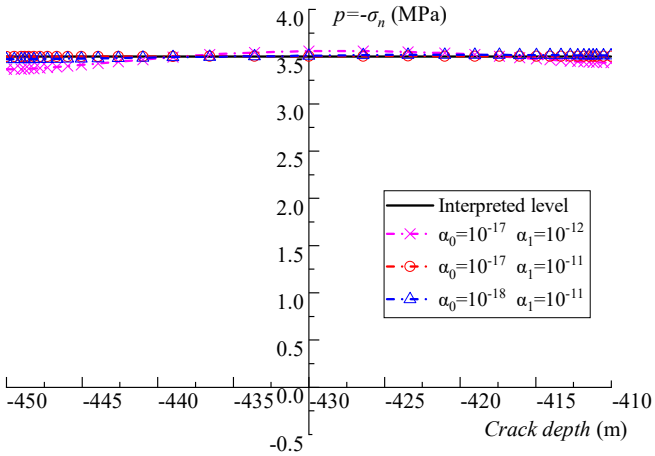

Fig. 15 The inversely solved net pressure applicable onto the fracture walls

The results show that the reservoir fracture pressure can be calculated inversely by only 15 monitoring points, when $\alpha_0^i = 10^{-17}$, $\alpha_1^i = 10^{-11}(i = 1,2)$ the stability and accuracy of the obtained solution are the best to assumption pressure. The pressure value of the left part of the curve, namely the lower part of the fracture, is larger than the right part, which confirms that after the fluid injected into the well, the lower part of the fracture is larger than the injection pressure of 3.5 MPa under the action of gravity; while the pressure of the upper part of the fracture is almost

equal to the injection pressure; meanwhile, the pressure at both ends of the fracture is small. This indicates that the injected fluid did not reach the crack tip completely. As known from experience that in the short-term hydraulic fracturing process, the pressure injected into the bottom of the well must be greater than the pressure at both ends of the fracture, so the result obtained by inverse calculation is consistent with the actual situation. It can be seen that inversion of reservoir pressure based on surface displacements can better reflect the real situation of fluid spreading due to its pressure effect within reservoir.

6 Discussion

Based on an open source-code of constant-element boundary element method, a corresponding LE-BEM code was developed. Combining LE-BEM code with space regularization method, the algorithm for solving inverse problem was developed to figure out the boundary loading of near-field structure from far field response measurements. Examples were used to verify the correctness and demonstrate the accuracy of the LE-BEM code by being compared with analytical solution, constant-element boundary element method and known monitoring data. Meanwhile the algorithm of inversion strategy was applied to analyzing the hydraulic fracturing treatment targeted at a coal seam in Canada, and the fracture pressure in coal seam was inversed, and the internal pressure mechanism was analyzed.

The inversion strategy combined with LE-BEM was applied to hydraulic fracturing engineering to effectively infer the inner pressure of a fracture from induced far-field deformation of the reservoir. The forward simulation of LE-BEM showed that the oblique reservoir fracture opened by a net pressure would introduce double humps with unequal height to ground surface.

Since the fracture was nearly vertical, considering that the elastic deformation was a free boundary, the fracture opened to both sides under the action of net pressure, the left and right swelling should be mainly upward deformation, while the fracture tip was located in the middle, and the deformation was offset or even subsidence due to the uplift of the twin peaks. In addition, because of the existence of angle, the differences in both sides of the deformation tendency of the fracture, the upper side medium mainly extruded to the upward, the other side of the medium extruded to the downward slightly. Compared with the infinite depth of the medium encountered by downward extrusion, the medium encountered by upward extrusion was limited to the surface, so the phenomenon of double peaks with unequal heights was presented.

Cai [24] used constant element BEM by setting 120 monitoring points to invert reservoir pressure. However, using LE-BEM code, only 15 monitoring points were required to reverse the higher-precision results, which indicates that this method is of great significance to improving inversion accuracy and engineering application.

At present, this strategy was developed by two-dimensional version developed on the fundamental solution of the infinite plane. In fact, three-dimensional analysis can calculate the pressure underground more accurately. The inverse problem solving strategy using the linear boundary element based on infinite plane fundamental solutions is proven to be feasible, and the extension of 3D researches based on the full-space and semi-space fundamental solutions are being planned as the near future work which can be expected to better facilitate the field application of this technique.

7 Conclusion

In order to reveal the geo-mechanical effects of geological storage process, a novel strategy of numerical solution was proposed to inverse the monitoring data of induced surface displacements using the linear-element boundary element method. The following conclusions are drawn:

The source code of two-dimensional LE-BEM was developed. The development as well as its validation with regards to planar elastic problems lays a solid foundation for its potential application and further extension to 3D analysis. The correctness and accuracy of the self-developed LE-BEM code were verified and demonstrated by comparing with the analytical solution and the constant element BEM code when these three had been used to solve the same problems. It was proved that the LE-BEM code was efficient and can further improve the simulation accuracy than the constant element BEM code.

The effectiveness of solution to inverse problem using LE-BEM was verified by a computational example: The model was a square plate with a square hole at its center whose bottom is fixed. The mid-symmetrically linearly distributed pressures which is loaded on the top boundary can be inversely figured out by just measuring the displacements at a few sampling positions within the plate.

The oblique reservoir fracture affected the trends of formation deformation. Under a net pressure on the walls, an absolutely vertical fracture underground causes the ground to deform as double humps with equal height, while a fracture with a certain dip angle causes surface to deform as double humps with unequal height, where the taller hump corresponded to the dip pointing side, and vice versa.

In engineering applications, it would be a novel attempt to infer equivalent reservoir boundary mechanical effects according to their induced surface displacements. The inverse solution strategy will improve our understanding on the mechanical aspect of the process during geological storage and lay a solid foundation for rationally analyzing the state of underground reservoirs.

Funding

This work was supported by the Open Research Fund of State Key Laboratory of Geomechanics and Geotechnical Engineering, Institute of Rock and Soil Mechanics, Chinese Academy of Sciences, under Grant [NO. SKLGME021021].

Disclosure statement

The authors report there are no competing interests to declare.

Data availability statement.

The datasets generated and/or analyzed during the current study are available from the corresponding author upon reasonable request.

References

[1] Sun, X., Zhang, L., & Zhang, B. (2021). Research on the coal industry development and transition in China under the background of carbon neutrality. *China Mining Magazine*, 30(02), 1-6. DOI: 10.12075/j.issn.1004-4051.2021.02.034.

[2] Li, N., Wang, J., & Liu, R., *et al.* (2021). Multi-scenario conception on the development of natural gas industry under the goal of carbon neutrality. *Natural Gas Industry*, 41(02), 183-192. DOI: 10.3787/j.issn.1000-0976.2021.02.021.

519 [3] Cho, S., Kim, S., & Kim, J. (2019). Life-cycle energy, cost, and CO_2 emission of CO_2-enhanced coalbed methane
520 (ECBM) recovery framework. *Journal of Natural Gas Science and Engineering*, 70, 102953. DOI:
521 10.1016/j.jngse.2019.102953.

522 [4] Pan, Z., Ye, J., & Zhou, F., *et al.* (2018). CO_2 storage in coal to enhance coalbed methane recovery: a review of
523 field experiments in China. *International Geology Review*, 60(5-6), 754-776. DOI:
524 10.1080/00206814.2017.1373607.

525 [5] Li, H., Zheng, L., & Liu, J. (2017). Full-field modeling and analysis of surface deformations induced by gas
526 injections into reservoirs. *Journal of Southwest Petroleum University (Science & Technology Edition)*, 39(03), 147-
527 157. DOI: 10.11885/j.issn.1674-5086.2015.03.06.02.

528 [6] Rizzo, J. (1967). An integral equation approach to boundary value problems of classical elastostatics. Q. Appl.
529 Math., 25, 83-95. DOI: 10.1090/qam/99907.

530 [7] Lachat, J., & Watson, J. (1976). Effective numerical treatment of boundary integral equations: a formulation for
531 three-dimensional elastostatics. *International Journal for Numerical Methods in Engineering*, 10(5), 991-1005.
532 DOI: 10.1002/nme.1620100503.

533 [8] Crouch, S. (1976). Solution of plane elasticity problems by the displacement discontinuity method. I. Infinite body
534 solution. *International Journal for Numerical Methods in Engineering*, 10(2), 301-343. DOI:
535 10.1002/nme.1620100206.

536 [9] Crouch, S., & Starfidld, A. (1983). Boundary element methods in solid mechanics. London, George Allen & Unwin.
537 DOI: 10.1016/0141-1187(83)90029-9.

[10] Yao, W., Yu, B., & Gao, X., *et al.* (2014). A precise integration boundary element method for solving transient heat conduction problems. *International Journal of Heat and Mass Transfer*, 78. DOI: 10.1016/j.ijheatmasstransfer.2014.07.029.

[11] Cui, X., Li, H., & Cheng, G., *et al.* (2017). Contour integral approaches for the evaluation of stress intensity factors using displacement discontinuity method. *Engineering Analysis with Boundary Elements*, 82, 119-129. DOI: 10.1016/j.enganabound.2017.05.008.

[12] Shou, K., & Napier, J. (1999). A two-dimensional linear variation displacement discontinuity method for three-layered elastic media. *International Journal of Rock Mechanics and Mining Sciences*, 36(6), 719-729. DOI: 10.1016/s0148-9062(99)00042-x.

[13] Crawford, A., & Currant, J. (1982). Higher-order functional variation displacement discontinuity elements. *International Journal of Rock Mechanics and Mining Sciences & Geomechanics Abstracts*, 3(19), 143-148. DOI: 10.1016/0148-9062(82)91154-8.

[14] Jeng, G., & Wexler, A. (1977). Isoparametric, finite element, variational solution of integral equations for three-dimensional fields. *International Journal for Numerical Methods in Engineering*, 11(9), 1455-1471. DOI: 10.1002/nme.1620110909.

[15] Korkut, L., & Mikelić, A. (1986). The potential integral for a polynomial distribution over a curved triangular domain. *International journal for numerical methods in engineering*, 23(12), 2277-2285. DOI: 10.1002/nme.1620231209.

[16] Assaad, M. (1983). Development of the linear displacement discontinuity method. *Iowa State University.* DOI: 10.31274/rtd-180813-7993.

[17] Gong, B., Wang, Y., & Zhao, T., *et al*. (2022,). AE energy evolution during CJB fracture affected by rock heterogeneity and column irregularity under lateral pressure. *Geomatics, Natural Hazards and Risk*, 13(1), 877-907. DOI: 10.1080/19475705.2022.2047114.

[18] Wong, L., & Cui, X. (2021). DDFS3D: A set of open-source codes leveraging hybrid 3D displacement discontinuity method and fictitious stress method to simulate fractures. *Engineering Analysis with Boundary Elements*, 131, 146-158. DOI: 10.1016/j.enganabound.2021.06.006.

[19] Rezvan, A., Mohammad, F., & Abolfazl, A., *et al.* (2021). Development of higher-order displacement discontinuity method to simulate fatigue crack growth in brittle materials. *Engineering Fracture Mechanics*, 258, 108087. DOI: 10.1016/j.engfracmech.2021.108087.

[20] Gu, Y., & Zhang, C. (2020). Novel special crack-tip elements for interface crack analysis by an efficient boundary element method. *Engineering Fracture Mechanics*, 239, 107302. DOI: 10.1016/j.engfracmech.2020.107302

[21] Chen, L., Lian, H., & Liu, Z., et al. (2019). Structural shape optimization of three dimensional acoustic problems with isogeometric boundary element methods. *Computer Methods in Applied Mechanics and Engineering*, 355, 926-951.DOI: 10.1016/j.cma.2019.06.012.

[22] Tarantola, A. (2005). Inverse problem theory and methods for model parameter estimation. *Society for Industrial and Applied Mathematics.* DOI: 10.1137/1.9780898717921.

[23] Maniatty, A., Zabaras, N., & Stelson, K. (1989). Finite element analysis of some inverse elasticity problems. *Journal of engineering mechanics*, 115(6), 1303-1317. DOI: 10.1061/(asce)0733-9399(1989)115:6(1303).

[24] Cai, S. (2015). Study on inverse problem from surface displacement monitoring to solving fluid injection into reservoir. Dalian University of Technology.

[25] Wang, Y. (2007). Computational methods for inverse problems and their applications. Higher Education Press.

[26] Tikhonov, A. (1963). On solving incorrectly posed problems and method of regularization. *Doklady Akademii Nauk USSR*, 151(03), 501-504.

[27] Landweber, L. (1951). An iteration formula for Fredholm integral equations of the first kind. *American journal of mathematics*, 73(3), 615-624.

[28] Zabaras, N., Morellas, V., & Schnur, D. (1989). Spatially regularized solution of inverse elasticity problems using the BEM. *Communications in applied numerical methods*, 5(8), 547-553. DOI: 10.1002/cnm.1630050808.

[29] Schnur, D., & Zabaras, N. (1990). Finite element solution of two-dimensional inverse elastic problems using spatial smoothing. *International Journal for Numerical Methods in Engineering*, 30(1), 57-75. DOI: 10.1002/nme.1620300105.

[30] Zhang, F., Kassab, A., & Nicholson, D. (1997). A boundary element solution of an inverse elasticity problem and applications to determining residual stress and contact stress. *International Journal of Solids and Structures*, 34(16), 2073-2086. DOI: 10.1016/s0020-7683(96)00152-7.

[31] Li, Q., Liu, G., & Zhang, J., *et al.* (2013). Status and suggestion of environmental monitoring for CO_2 geological storage. *Advances in Earth Science*, 28(6), 718-727. DOI: 10.11867/j.issn.1001-8166.2013.06.0718.

[32] Zhang, Q., Cui, Y., & Bu, X. (2011). Analysis of development status of CCS monitoring technology. *Shenhua science and technology*, (2), 77-82.

[33] Vasco, D., Ferretti, A., & Novali, F. (2008). Reservoir monitoring and characterization using satellite geodetic data: Interferometric synthetic aperture radar observations from the Krechba field, Algeria. *Geophysics,* 73(6), WA113-WA122. DOI: 10.1190/1.2981184.

598 [34] Zheng, L. (2015). Full-field modeling and analysis of surface deformations induced by gas injections into
599 reservoirs. Dalian University of Technology.

600 [35] Sneddon, I. (1951). Fourier transforms. New York, McGraw-Hill.

601 [36] Li, S., He, T. & Yin, X. (2010). Introduction of Rock Fracture Mechanics. *University of Science and Technology*
602 *of China Press.*

603 [37] Li, H., Mizuta, Y. & Kyoizumi, N. (2001). Parabolic crack-tip element of two-dimensional displacement
604 discontinuity methods with complete analytical integrations realized by algebraic manipulation. *The 38th U.S.*
605 *Symposium on Rock Mechanics (USRMS), Washington, D.C.*

Appendix A

Kernel function $f(x,y)$ is linear integral of $(D_i * g)$, expressed as:

$$f(x,y) = \int_{x_i}^{x_{i+1}} N_1 D_i^1 * g(x-\xi,y)d\xi + \int_{x_i}^{x_{i+1}} N_2 D_i^2 * g(x-\xi,y)d\xi = D_i^1 * f_1(x,y) + D_i^2 * f_2(x,y) \quad (A.1)$$

Substitute N_1 and N_2 into the above equation to get:

$$f_1(x,y) = \int_{x_i}^{x_{i+1}} \left(\frac{\xi - x_{i+1}}{x_i - x_{i+1}}\right) g(x-\xi,y)d\xi \quad (A.2)$$

$$f_2(x,y) = \int_{x_i}^{x_{i+1}} \left(\frac{\xi - x_i}{x_{i+1} - x_i}\right) g(x-\xi,y)d\xi \quad (A.3)$$

For odd nodes on the element, x_i and x_{i+1} are *-1/2a* and *3/2a*, respectively. For even-numbered nodes x_i and x_{i+1} are *-3/2a* and *1/2a*, respectively.

By the calculation, $f_1(x,y)$ and $f_2(x,y)$ on the odd-numbered nodes are expressed as:

$$f_1(x,y) = -C_1\{[(x-1.5a)^2 - y^2]\ln[(x-1.5a)^2 + y^2] - [(x+0.5a)(x-3.5a) - y^2]\ln[(x+0.5a)^2 + y^2] - 4y(x-1.5a)T_1 + 4a(x-2.5a)\} \quad (A.4)$$

$$f_2(x,y) = C_1\{[(x+2.5a)(x-1.5a) - y^2]\ln[(x-1.5a)^2 + y^2] - [(x+0.5a)^2 - y^2]\ln[(x+0.5a)^2 + y^2] - 4y(x+0.5a)T_1 + 4a(x+1.5a)\} \quad (A.5)$$

$f_1(x,y)$ and $f_2(x,y)$ on the even-numbered nodes are expressed as:

$$f_1(x,y) = -C_1\{[(x-0.5a)^2 - y^2]\ln[(x-0.5a)^2 + y^2] - [(x+1.5a)(x-2.5a) - y^2]\ln[(x+1.5a)^2 + y^2] - 4y(x-0.5a)T_2 + 4a(x-1.5a)\} \quad (A.6)$$

$$f_2(x,y) = C_1\{[(x+3.5a)(x-0.5a) - y^2]\ln[(x-0.5a)^2 + y^2] - [(x+1.5a)^2 - y^2]\ln[(x+1.5a)^2 + y^2] - 4y(x+1.5a)T_2 + 4a(x+2.5a)\} \quad (A.7)$$

where, $C_1 = [32\pi(1-v)a]^{-1}$, $T_1 = \tan^{-1}[y/(x-1.5a)] - \tan^{-1}[y/(x+0.5a)]$, $T_2 = \tan^{-1}[y/(x-0.5a)] - \tan^{-1}[y/(x+1.5a)]$.

Similarly, integrate every derivative of $g(x,y)$ to the derivatives of $f_1(x,y)$: $f_{1,x}, f_{1,y}, f_{1,xx}, f_{1,xy}, f_{1,yy}, f_{1,xxx}, f_{1,xxy}, f_{1,xyy}, f_{1,yyy}$ and the derivatives of $f_2(x,y)$: $f_{2,x}, f_{2,y}, f_{2,xx}, f_{2,xy}, f_{2,yy}, f_{2,xxx}, f_{2,xxy}, f_{2,xyy}, f_{2,yyy}$.

For odd-numbered nodes, the derivatives of $f_1(x,y)$ and $f_2(x,y)$ are expressed as:

$$f_{1,x} = -4C_1[(x-1.5a)L_1 - yT_1 + 2a] \tag{A.8}$$

$$f_{2,x} = 4C_1[(x+0.5a)L_1 - yT_1 + 2a] \tag{A.9}$$

$$f_{1,y} = 4C_1[yL_1 + (x-1.5a)T_1] \tag{A.10}$$

$$f_{2,y} = -4C_1[yL_1 + (x+0.5a)T_1] \tag{A.11}$$

$$f_{1,xy} = 4C_1(T_1 - 2ayA_1) \tag{A.12}$$

$$f_{2,xy} = -4C_1(T_1 - 2ayB_1) \tag{A.13}$$

$$f_{1,yy} = -f_{1,xx} = 4C_1[L_1 + 2a(x+0.5a)A_1] \tag{A.14}$$

$$f_{2,yy} = -f_{2,xx} = -4C_1[L_1 + 2a(x-1.5a)B_1] \tag{A.15}$$

$$f_{1,xyy} = -f_{1,xxx} = -4C_1\{[(x+2.5a)(x+0.5a)^2 + (x-1.5a)y^2]A_1^2 - (x-1.5a)B_1\} \tag{A.16}$$

$$f_{2,xyy} = -f_{2,xxx} = -4C_1\{[(x-3.5a)(x-1.5a)^2 + (x+0.5a)y^2]A_1^2 - (x+0.5a)B_1\} \tag{A.17}$$

$$f_{1,yyy} = -f_{1,xxy} = -4C_1\{[(x+0.5a)(x+4.5a) + y^2]A_1^2 - B_1\} \tag{A.18}$$

$$f_{2,yyy} = -f_{2,xxy} = -4C_1\{[(x-1.5a)(x-5.5a) + y^2]A_1^2 - B_1\} \tag{A.19}$$

For even-numbered nodes, the derivatives of $f_1(x,y)$ and $f_2(x,y)$ are expressed as:

$$f_{1,x} = -4C_1[(x-0.5a)L_2 - yT_2 + 2a] \tag{A.20}$$

$$f_{2,x} = 4C_1[(x+1.5a)L_2 - yT_2 + 2a] \tag{A.21}$$

$$f_{1,y} = 4C_1[yL_2 + (x-0.5a)T_2] \tag{A.22}$$

$$f_{2,y} = -4C_1[yL_2 - (x+1.5a)T_2] \tag{A.23}$$

$$f_{1,xy} = 4C_1(T_2 - 2ayA_2) \tag{A.24}$$

$$f_{2,xy} = -4C_1(T_2 - 2ayB_2) \tag{A.25}$$

$$f_{1,yy} = -f_{1,xx} = 4C_1[L_2 + 2a(x+1.5a)A_2] \tag{A.26}$$

$$f_{2,yy} = -f_{2,xx} = -4C_1[L_2 + 2a(x-0.5a)B_2] \tag{A.27}$$

$$f_{1,xyy} = -f_{1,xxx} = -4C_1\{[(x+3.5a)(x+1.5a)^2 + (x-0.5a)y^2]A_2^2 - (x-0.5a)B_2\} \tag{A.28}$$

$$f_{2,xyy} = -f_{2,xxx} = -4C_1\{[(x-2.5a)(x-0.5a)^2 + (x+1.5a)y^2]A_2^2 - (x+1.5a)B_2\} \tag{A.29}$$

$$f_{1,yyy} = -f_{1,xxy} = -4C_1\{[(x+1.5a)(x+5.5a) + y^2]A_2^2 - B_2\} \tag{A.30}$$

$$f_{2,yyy} = -f_{2,xxy} = -4C_1\{[(x-0.5a)(x-4.5a) + y^2]A_2^2 - B_2\} \tag{A.31}$$

where, $L_1 = \log\sqrt{(x-1.5a)^2+y^2} - \log\sqrt{(x+0.5a)^2+y^2}$, $L_2 = \log\sqrt{(x-0.5a)^2+y^2} - \log\sqrt{(x+1.5a)^2+y^2}$, $A_1 = [(x+0.5a)^2+y^2]^{-1}$, $B_1 = [(x-1.5a)^2+y^2]^{-1}$, $A_2 = [(x+1.5a)^2+y^2]^{-1}$, $B_2 = [(x-0.5a)^2+y^2]^{-1}$.